

Initiating crystal growth kinetics of α -HC(NH₂)₂PbI₃ for flexible solar cells with long-term stability

Jun Xi ^{a,1}, Zhaoxin Wu ^{a,*1}, Kai Xi ^{b,1}, Hua Dong ^a, Bin Xia ^a, Ting Lei ^a, Fang Yuan ^a, Wen Wu ^a, Bo Jiao ^a, Xun Hou ^a

^a Key Laboratory of Photonics Technology for Information, Key Laboratory for Physical Electronics and Devices of the Ministry of Education, School of Electronic and Information Engineering, Xi'an Jiaotong University, Xi'an 710049, PR China

^b Department of Materials Science and Metallurgy, University of Cambridge, Cambridge CB3 0FS, UK

ARTICLE INFO

Article history:

Received 10 January 2016
Received in revised form
5 June 2016
Accepted 6 June 2016
Available online 7 June 2016

Keywords:

Formamidinium lead iodide
Crystal growth kinetics
Thermal energy
Flexible solar cells
Long-term stability

ABSTRACT

Flexible and stable energy conversion devices are core components for next generation flexible electronics. Perovskite solar cells using formamidinium lead iodide (FAPbI₃) exhibit superior power conversion efficiency (PCE), but the strenuous process of n-i-p configuration and the instability of α -FAPbI₃ become inevitable obstacles for practical application in flexible electronics. Here, we for the first time report the particular crystal growth process of α -FAPbI₃ grain with a controlled size for the development of flexible perovskite solar cells. Through morphology, element and thermostability measurements, the crystalline size and film homogeneity are found to mainly depending on decent thermal energy and doping density of methylammonium bromine. Additionally, stable "pseudocubic" lattice with larger crystalline size is established owing to the varied tolerance factor. We demonstrated that the flexible solar cells exhibiting an average PCE of $12.41 \pm 0.52\%$ (the optimal 13.03%), which slightly decreased to $10.98 \pm 1.00\%$ (the optimal 12.0%) over one month at 35% humidity without encapsulation, based on the modified α -FAPbI₃ for most efficient devices. This work favors the understanding of the crystal growth kinetics of α -FAPbI₃ for flexible substrate, and paves the way for potential application of flexible electronics.

© 2016 Elsevier Ltd. All rights reserved.

1. Introduction

Hybrid organic-inorganic perovskite has recently been studied and developed into a superb light harvester since Miyasaka pioneered an efficiency of 3.81% [1]. Perovskite, based on organometal halide (ABX₃), shows high absorption coefficient, long-rang carrier transport and proper bandgap [2–5]. Recently, an ultrahigh certified power conversion efficiency (PCE) of 20.1% has been reported by Seok, which is comparable to polycrystalline Si cells [6].

With respect to the typical structure of ABX₃ (B=Pb or Sn, X=Cl, Br or I) perovskite, the tolerance factor (*t*) [7] defined formerly, $t=(r_A+r_B)/[2^{1/2}(r_B+r_X)]$, is employed to evaluate the perovskite formation, where *r*_A is the radius of the organic cation (such as CH₃NH₃⁺, (NH₂)₂CH₂⁺ and so on), *r*_B is the radius of Pb²⁺ or Sn²⁺, *r*_X is the radius of the halogen anion (such as I[−], Br[−], or Cl[−]). The perovskite bandgap can hence be tailored by various ions substitutions. In term of the perovskite containing Sn²⁺, the

absorption edge of corresponding films can be pushed to infrared light (> 1000 nm), indicating more suitable bandgap (1.1–1.4 eV) for single-junction cells [8–10]. In addition, the bandgap can be adjusted from 1.6 eV to 2.3 eV by replacing I with varied halid anion X (Br or Cl) for virgin CH₃NH₃PbI₃ [11–14], which is favorable for tandem cells with III-V inorganic semiconductors [15]. As for CH₃NH₃⁺ (MA⁺), the organic cation A, it commonly occupies the position of general crystal structure and establishes a tetragonal structure rather than a cubic one [16,17]. More importantly, a majority of superior perovskite solar cells have been prepared based on MAPbI₃ or MAPbI_{3-x}Cl_x [18–20]. Nevertheless, these devices are apt to decay in ambient air due to the tilting lattice containing MA⁺. From the tolerance factor *t*, a slightly larger cation A could improve the lattice structure symmetry as well as stability. If the crystal structure involved with much larger cation A (such as CH₃CH₂NH₃⁺), a layered (two-dimensional) structure will be adopted rather than steric (three-dimensional) one for the prepared perovskite [21]. Mitzi proved that the formamidinium (HC(NH₂)₂⁺=FA⁺) with larger size can form stable structure in hybrid tin iodide perovskite [22,23]. A reduced bandgap (1.47 eV) of FAPbI₃ was obtained afterwards, which implies greater capacity for sunlight absorption than MAPbI₃ (1.55 eV) [24]. Further studies

* Corresponding author.

E-mail address: zhaoxinwu@mail.xjtu.edu.cn (Z. Wu).

¹ These authors contributed equally.

have shown two polymorphs existing in FAPbI₃: black trigonal perovskite (α -phase) above 160 °C and yellow hexagonal non-perovskite (δ -phase) at room temperature. In addition, the carrier diffusion lengths of α -FAPbI₃ were previously estimated to about 177 nm and 813 nm for electrons and holes, respectively [25]. Several groups have reported outstanding efficiency (up to 17.9%) based on FAPbI₃ or its mixture [25–29]. However, the high temperature of TiO₂ process in this n-i-p configuration has hindered the promotion of popular flexible devices [30–34]. In the meanwhile, planar heterojunction (PHJ) devices with p-i-n architecture for FAPbI₃ are seldom studied due to the instability of α -phase at room temperature. As is known, the device performance significantly relies on the perovskite crystalline grains, which will substantially impact the carriers transport and charge traps [35]. The mechanism of MAPbI₃ or MAPbI_{3-x}Cl_x crystal growth has been widely explored by diverse methods [19,36,37]. Unfortunately, the research involving the process of crystal nucleation and growth of α -FAPbI₃ is scanty. Encouraged for future commercial potential with this amusing material, we are provoked to discover the crystal growth kinetics of α -FAPbI₃ film on the flexible substrates.

By thoroughly investigating the nature of the modified α -FAPbI₃ (doping with MABr) film upon tin-doped indium oxide deposited on polyethylene naphthalate (ITO-PEN) substrate, we unveiled the crystal growth kinetics intensely depending on the temperature and the doping ratio. (Although Seok [38] has reported the α -FAPbI₃ assisted by little MABr, the elaborate role of MABr is ambiguous.) Notably, the pristine lattice could be reinforced at a mild temperature region and the crystal domain could be expanded as doping ratio increase. Moreover, the crystal lattice was contracted to be stable “pseudocubic”. Finally, we realized highly efficient flexible perovskite solar cells composed of ITO-PEN substrate, poly(3,4-ethylenedioxythiophene) polystyrene sulfonate (PEDOT:PSS) hole transfer layer, modified α -FAPbI₃ layer, ((6,6)-phenyl-C61-butrylic acid methyl ester)-(2,9-dimethyl-4,7-diphenyl-1,10-phenanthroline) ((PCBM)-(BCP)) electron transfer layer and Ag as the cathode. Employing a profitable film and bandgap of α -FAPbI₃, an optimal efficiency of 13.03% (average efficiency of 12.41 ± 0.52%) was achieved for flexible solar cells, whose stability was almost extended beyond one month at 35% humidity.

2. Experimental section

2.1. Preparation of materials

Formamidinium iodide (FAI) was synthesized by following previous literature [25]. In brief, formamidinium acetate ($\geq 98.0\%$, Sigma Aldrich) was dissolved in 10 mL hydriodic acid (57 wt% in water, Sigma Aldrich) in a molar ratio of 1:2 in a 50 mL round bottom flask by constant stirring at 50 °C for 10 min. The precipitate was gained by rotary evaporation at 100 °C and washed with dry diethyl ether until the solid became white. Methylammonium bromide (MABr) was synthesized in a similar way: 24 mL methylamine solution (33 wt% in ethanol, Sigma Aldrich) and 10 mL hydrobromic acid (48 wt% in water, Sigma Aldrich) were diluted by 100 mL ethanol at 0 °C for 2 h. The final precipitate was obtained by a same process. PbI₂ (99.999 wt%) was purchased from Alfa. PEDOT:PSS (CLEVIOS pH 1000) solution and PCBM were acquired from Heraeus and Solenne, respectively.

2.2. Fabrication of solar cells

ITO-PEN substrates were cleaned sequentially by detergent, pure water, acetone for 20 min. The dried substrates were treated

with ultraviolet ozone plasma for 5 min for further clean. PEDOT:PSS solution (dissolved with deionized water in a mixture ration of 1:3) were spun at 1000 rpm for 30 s and annealed at 120 °C for 20 min. We transferred the substrates coated PEDOT:PSS to a vacuum chamber. The PbI₂ film of 40 nm was sublimated under a pressure of 10⁻⁵ mbar at a rate of 1.0 Å/s and resultant substrates were placed into the N₂-filled glovebox. Heated for 1 min at 60 °C, drops of 0.063 mol/L FAI, MABr solution or mixture of thereof (4:1, 3:1, 2:1, 1:1 and 0:1) solution in 2-propanol were loaded for 10 s, and then spin-coated at 2000 rpm on the ITO/PEDOT:PSS/PbI₂ substrate for 20 s. Afterwards, the prepared films were drying at 90 °C, 120 °C and 150 °C for 10 min, respectively. To remove the unreacted excess of FAI or MABr, 2-propanol solvent was spun at 2000 rpm upon the perovskite film for 1 min. The final film was annealed at 120 °C for 5 min. The preparation of next layer was implemented in a same process until the required thickness was achieved. Annealed at 100 °C for 20 min, the hybrid perovskite film was further crystallized and inner-interface would be removed. Eventually, the devices were completed by consecutively vacuum deposited PCBM (15 nm), BCP (6 nm) and Ag cathode (120 nm) under 10⁻⁵ mbar.

2.3. Characterization

The absorption spectra were acquired on a UV-vis spectrophotometer (Fluoromax 4, HORIBA Jobin Yvon, USA). The morphology was investigated by a scanning electron microscopy (SEM) (Quanta 250, FEI). The transmission electron microscope (TEM) images were recorded on a FEI Tecnai G2 F30 S-Twin at an accelerating voltage of 300 kV. The elemental composition in the corresponding films was measured by EDX with Standardless Quantification Model. The EDX spectra of overall perovskite films were obtained at a dwell time of 100 μs and 5 eV/channel with a 20 kV accelerating voltage. The crystalline structures were performed by a X-ray diffraction (XRD) (D/MAX-2400, Rigaku, Japan) with Cu K α radiation. The hybrid perovskite powders peeled off from the substrates, were analyzed by thermogravimetric analysis (TGA) with Mettler-Toledo TGA Instrument using a 5 °C/min ramp up to 300 °C in N₂ atmosphere with a steady flow rate of 10 mL/min.

Device characteristics were evaluated in ambient under a AAA solar simulator (XES-301S, SAN-EI Electric. Co. Ltd.), AM 1.5G illumination with an intensity of 100 mW/cm². The current density-voltage (*J-V*) curves were measured by a Keithley digital source meter (Model 2602). For the inverted PHJ devices, the scan rates of current-voltage curves were performed by 0.5 V/s starting from -0.1 V to 1.2 V. The Incident Photon-to-current Conversion Efficiency (IPCE) spectra were obtained by the solar cell quantum efficiency measurement system (SolarCellScan 100, Zolix instruments. Co. Ltd.). The area of each device, calibrated by the shadow mask, was 9.00 mm².

3. Results and discussion

A modified 2-step deposition was applied to prepare the α -FAPbI₃ film with MABr. The schematic picture is shown in Fig. 1(a), and the details can be found in the experimental section. First PbI₂ was sublimated in the vacuum chamber onto the ITO-PEN substrate (purchased from Peccell Tech.) covered with PEDOT:PSS layer to form a 40 nm transparent yellow film. Next the substrate was heated at 60 °C for 1 min, droplets of FAI/MABr (4:1, 3:1, 2:1, 1:1) solution in total 0.063 mol/l were dripped upon the PbI₂ film for 10 s and then spun to form a battery of films. The PbI₂-(FAI/MABr) bilayer was annealed at different temperatures (90 °C, 120 °C and 150 °C) form into a 100 nm α -FAPbI₃ with black polymorphs by *in situ* by inter-diffusion, which permitted elimination

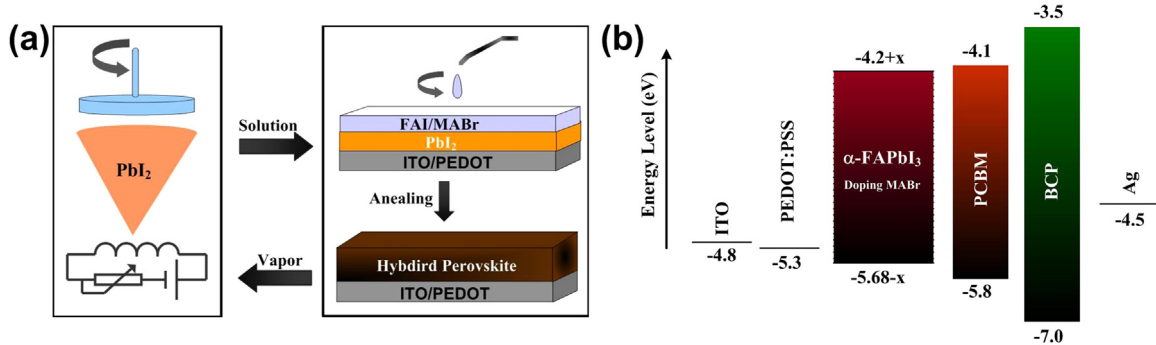


Fig. 1. (a) Schematic process of the hybrid perovskite deposition. (b) Device configuration and corresponding energy levels diagram.

of the pristine PbI_2 film. Residual FAI/MABr on the perovskite film was cleaned by spinning 2-propanol on the substrate and annealed at 120 °C afterwards. This vapor-spinning process was implemented for 3 times for developing multilayer perovskite films (300 nm). MAPbI₂Br perovskite was also obtained by reacting PbI_2 with MABr. Eventually the PHJ device was completed via capping the perovskite film with PCBM (15 nm)/BCP (6 nm) and Ag (120 nm) cathode by vacuum deposition. The ultra-thin ETLs would ensure short carriers transport distance for reaching the Ag cathode. Fig. 1(b) depicts the energy levels diagram. The cross-sectional SEM images of the overall perovskite films and the final device shown in Fig. S1 confirmed the thickness of about 300 nm.

To justify the positive role of MABr agent, the surface morphologies of the perovskite films with varied MABr doping ratios at different temperatures are shown in Fig. 2. From left to right, the MABr doping ratio is increased from 1/5 to 1/2.

Intriguingly, the crystal size constantly increased as the doping ratio increased (except for the cold region). The oddly similar crystalline size of the cold region probably derived from the lower growth rate, which was deduced from the analogous grain growth of MAPbI₂Br (Fig. S2). Initially, it could be surmised that the crystal growth of the overall modified perovskite films is predominantly driven and accelerated by the MABr agent. This variation presumably arises from alteration of the crystal lattice and will be discussed later. As for the annealing condition, we intentionally define three thermal regions: cold (90 °C), mild (120 °C) and hot (150 °C). From cold to hot, the crystalline grains were also linearly enlarged, especially for the high concentration of doping ratio. It can be interpreted by the enhanced driving force which stimulates the crystal growth with the more thermal energy. On one hand, lower temperatures would allow too many solvents to limit the crystal growth. This led to irregular crystal shapes formation and

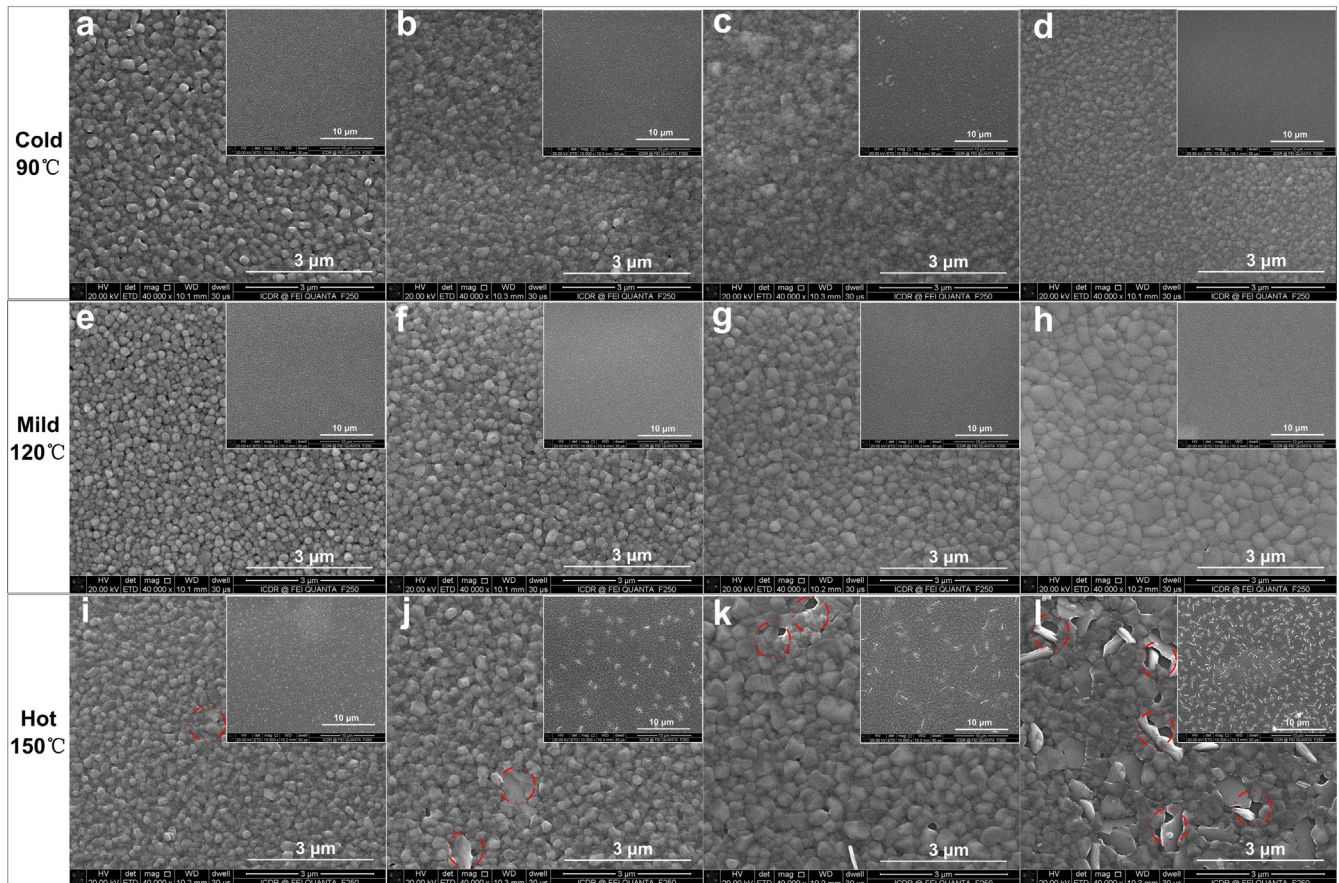


Fig. 2. Top-view SEM images of three controlled thermal regions by varied doping ratios. In each row, the doping ratio is 1/5, 1/4, 1/3 and 1/2, respectively. The inset of the image is the low magnification. (The red circles marked in the hot region are micro cracks, such as pinholes and voids.)

eventually caused loosen interaction between each crystalline grain which may lead to inferior interfaces in devices. On the other hand, high temperatures could over accelerate the growth speed due to “supersaturated solution” of perovskite film. Notably, lots of pinholes have been developed in the perovskite layer in the hot region and gradually increased and amplified as doping ratio increase. The inapprehensive results may be attributed to Br^- as some gas (eg. MABr) released from collapsed lattice at 150 °C. As for the mild region, homogeneous crystalline grains and uniform films were realized regardless of doping ratio.

To distinguish the released gas in hot region, we devised an intriguing experiment shown in Fig. S3(a): First, the modified perovskite films with various doping ratios were placed on a hot plate by annealing at 150 °C (the hot region). Then, a 40 nm evaporating PbBr_2 film adhered to a closed glass Petri dish was exposed to the different perovskite films to monitor the MABr release. The distance between the Petri dish and the perovskite film is about 3 cm. The PbBr_2 films after 2 h exposure are shown in Fig. S3(b) (the photo from top to down is the original PbBr_2 film, the changed PbBr_2 film exposed to perovskite film by 1/5 doping, 1/4 doping, 1/3 doping and 1/2 doping, respectively). We could see the azury PbBr_2 film became light yellow, and the color gradually became dark as the doping ratios increased. Furthermore, the corresponding XRD patterns of these films can be found in Fig. S3(c). Amusingly, the peak of 14.88° ((110) plane of MAPbBr_3) was gradually strengthened as the doping ratio increased, indicating more released MABr gas. From this interesting experiment, it could be deduced that the formation of pinholes is caused by MABr gas release during heating period.

To further demonstrate that various thermal regions are dominated by the MABr agent, the transmission electron microscope (TEM) – energy dispersive X-ray (EDX) spectroscopy was applied and the atomic percentages of Pb, I and Br dispersed in the perovskite films are shown in Fig. S4. The atomic ratio (I/Br) variation along the thermal regions change was depicted to intuitively elucidate the thermostability (Fig. 3(a)). The ratios are deviated from the operational solutions. The unexpected result probably originates from the discriminating reaction rate of FAI and MABr. Interestingly, the atomic ratios (I/Br) had an apparent trend, they reduced from cold to mild first and then increased from mild to hot, which was in agreement with the morphologies change. The degree of decay (Table S1) from mild to hot was gradually enhanced by 0.41, 0.53, 0.58 and 0.62 as MABr doping ratio increased. These results suggest that the hybrid perovskite $\text{FAPbI}_3 \cdot \text{MABr}$ is thermally unstable than the pure $\alpha\text{-FAPbI}_3$ as doping ratio increase. The distributions of Pb, I and Br were displayed by

elemental maps in Fig. S5. It was apparent that these primary elements were homogeneously distributed throughout the hybrid perovskite film, indicating superior film formation.

In Fig. 3(b), the TGA analysis was virtually conducted by the scraped powders of these films $\alpha\text{-FAPbI}_3$, $\text{FAPbI}_3 \cdot \text{MABr}$ (that is FAPbI_3 by 1/2 doping MABr) and MAPbI_2Br with thickness of about 1 μm , which were prepared by repeating evaporating PbI_2 (40 nm) and sequentially spin-coating FAI, FAI/MABr (1/1) and MABr (0.063 mol/l) for 10 times, respectively. It could be observed that the modified perovskite ($\text{FAPbI}_3 \cdot \text{MABr}$) decomposed through a two-step progress (170 °C as well as 240 °C). The initial decomposing temperature of $\text{FAPbI}_3 \cdot \text{MABr}$ is closely connected with the formed holes/pores of the annealing films at 150 °C, chiefly caused by MABr gas release. This little discrepancy between 150 °C and 170 °C may originate from the distinct surface areas between powder and film. Coincidentally, MAPbI_2Br and $\alpha\text{-FAPbI}_3$, both served as the contrastive materials, started to decompose at 170 °C and 240 °C, which are identical with the ones of some reports [13,39], implying lower thermostability as well as higher thermostability, respectively. Accordingly, the two decomposing stages of $\text{FAPbI}_3 \cdot \text{MABr}$ naturally proved the modified perovskite as a thermally binary alloy composing of MAPbI_2Br and $\alpha\text{-FAPbI}_3$. Besides, $\alpha\text{-FAPbI}_3$ can be easily converted into non-perovskite yellow phase ($\delta\text{-FAPbI}_3$) below 150 °C to damage the device performance [24]. The insight to the thermal property fundamentally revealed that MABr could weaken the high thermostability of $\alpha\text{-FAPbI}_3$ to readily facilitate the film crystal growth at lower temperatures, which is most available for flexible devices.

It is speculated that the crystal lattice could be stimulated by the mild agent from the SEM images. The modified $\alpha\text{-FAPbI}_3$ films at the mild region (120 °C) were selected to study the lattice transformation by X-ray diffraction (XRD) patterns. The integrated original XRD patterns and the fitting XRD patterns can be found in Fig. S6. Fig. 4(a) illustrates the XRD patterns in the enlarged ranges of 13.8–14.8° and 27.5–30.0° with increasing doping ratio. The full width at half maximum (FWHM) of the predominant peak in perovskite films with various MABr doping ratio (0, 1/5, 1/4, 1/3, 1/2 and 1) is 0.178, 0.144, 0.132, 0.117, 0.108 and 0.094, respectively, revealing promoted crystal growth driven by MABr, which was also reflected by the SEM images. Importantly, the main diffraction peaks were shifted from 13.9° to 14.6° and from 28.0° to 29.5° as the material changed from $\alpha\text{-FAPbI}_3$ to MAPbI_2Br . This indicates that a crystal transformation from the trigonal lattice with (110) and (220) planes to the cubic lattice with (100) and (200) planes took place. Therefore, a comparable stable structure can be anticipated for the “pseudocubic” lattice of hybrid $\text{FAPbI}_3 \cdot \text{MABr}$ due

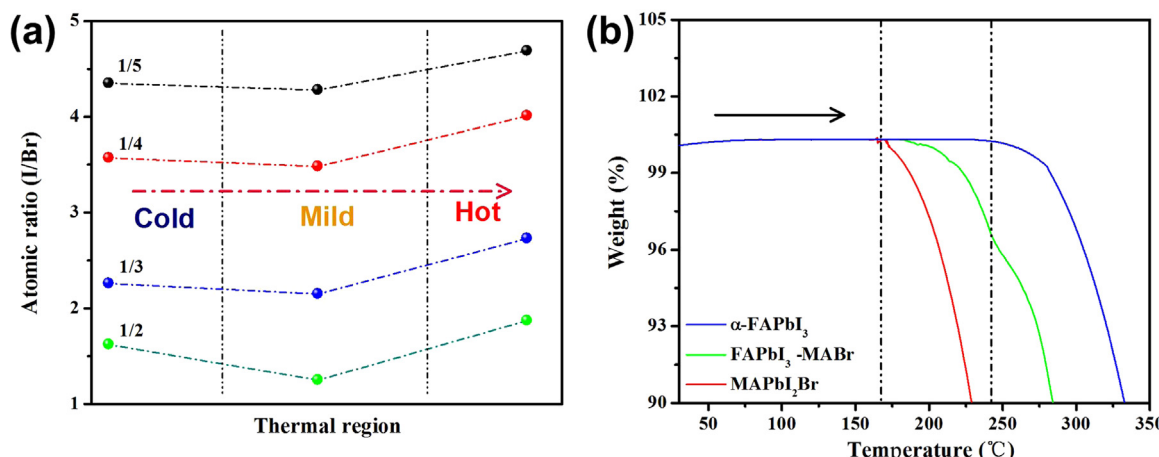


Fig. 3. (a) The variation of atomic ratio of (iodide/bromide) distributed in the hybrid perovskite films by TEM-EDX. (b) Thermogravimetric analysis of $\alpha\text{-FAPbI}_3$, MAPbI_2Br and $\text{FAPbI}_3 \cdot \text{MABr}$ (1/2 doping) from room temperature to 350 °C.

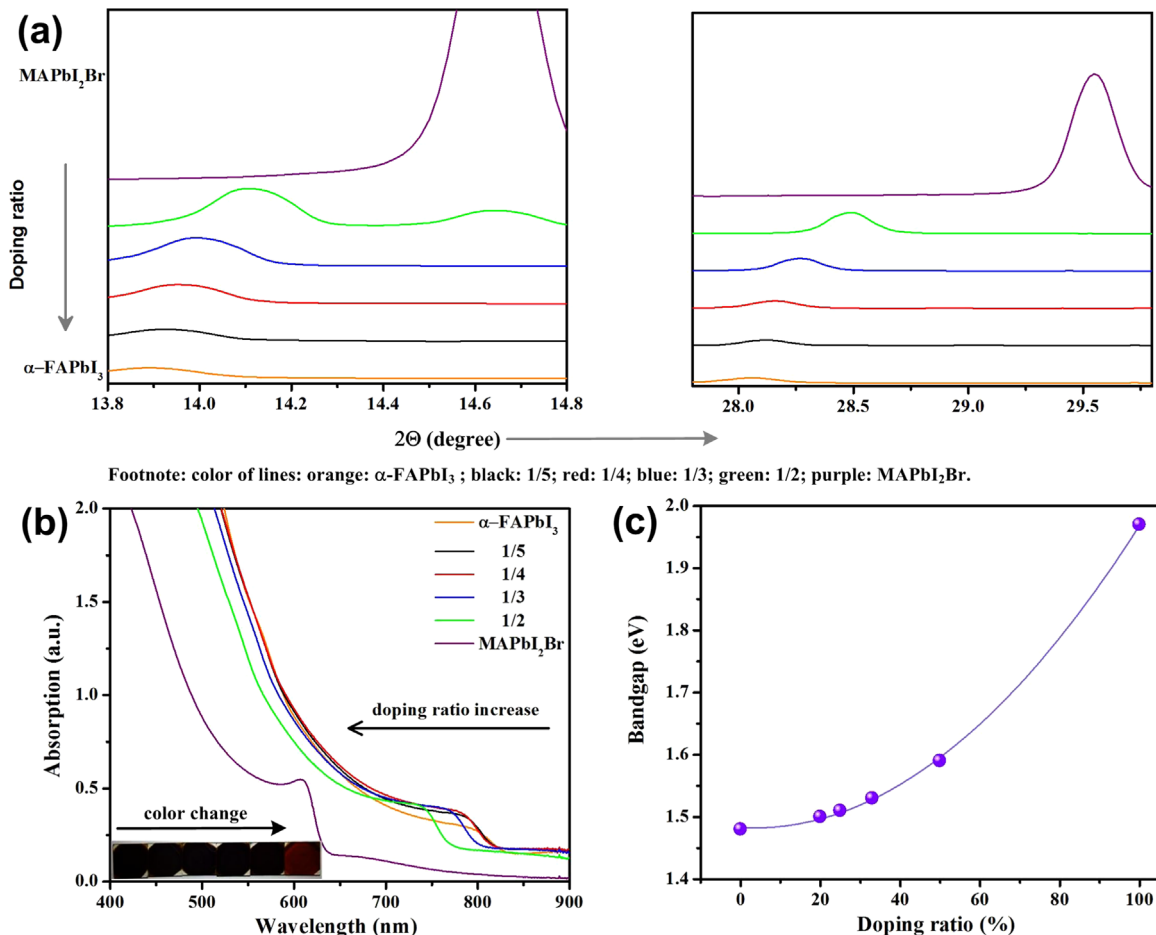


Fig. 4. The property transformation of the primitive $\alpha\text{-FAPbI}_3$ by mildly doping MABr. (a) Magnified XRD patterns in the ranges of 13.8–14.8° and 27.5–30.0°. (b) UV-vis absorption spectra of ITO/PEDOT:PSS/Perovskite. The colors of films shown as the inset of the photo. (c) An estimated curve of the modified bandgap as a function of doping ratio.

to insertion of MA^+ and Br^- into the pristine lattice frame. The change in lattice structure can be predicted from the equation of the tolerance factor t . The radius of the component ions Pb^{2+} , FA^+ , MA^+ , I^- and Br^- is 1.19 Å, 1.9 Å, 1.8 Å, 2.2 Å and 1.96 Å, respectively. Consequently, the t is estimated as 0.855 and 0.837 for $\alpha\text{-FAPbI}_3$ and MAPbI_2Br . The radius of A and X in the mixed lattice APbX_3 can be simply defined as the average size (such as $r_A = (r_{\text{FA}} + r_{\text{MA}})/2$, $r_X = (r_{\text{I}} + r_{\text{Br}})/2$ with a 50% doping ratio). The modified tolerance factor should be calculated as 0.853, 0.852, 0.851 and 0.849 when the doping ratio is 1/5, 1/4, 1/3 and 1/2, respectively. We could find that the value of t is gradually decreased as the doping ratio increased, which demonstrated the formation of “pseudocubic” lattice as well. It is also known that the most favorable t for maintaining the perovskite lattice is from 0.8 to 0.9 [40]. The modified $\alpha\text{-FAPbI}_3$ crystal lattice could be best established by the introduction of MABr, which is consistent with the report by Snaith et al. [25].

We realized that the bandgap of the modified $\alpha\text{-FAPbI}_3$ will be tuned by introducing mild MABr agent due to differing spin orbital coupling between Pb-I and Pb-Br [17]. To determine the variation of tailoring bandgap, the UV-visible absorption spectra of modified $\alpha\text{-FAPbI}_3$ are shown in Fig. 4(b). The onset of absorption band was evidently blue shifted as the doping ratio increased from 0 to 100%. The color of the film was also shifted from black to crimson (inset of Fig. 4(b)). A quadratic curve for the nonlinear variation of bandgap is hence plotted (Fig. 4(c)). This result also indicates that the bandgap will be facilely expanded by doping MABr, which is consistent with the variation of XRD patterns. The widened

bandgap is also accompanied by simultaneously elevated the lowest unoccupied molecular orbital (LUMO) and declined the highest occupied molecular orbital (HOMO), which would further affect energy level alignment in the interface.

To analyze various films, the PEDOT:PSS/modified $\alpha\text{-FAPbI}_3/\text{PCBM-BCP}$ flexible devices upon ITO-PEN substrates were prepared to demonstrate the effect of the temperature as well as the doping ratio. The corresponding device parameters are summarized in Table 1.

From Fig. 5(a) to (c), the J - V characteristics of various doping ratios in the three distinct thermal regions are exhibited. The EQE spectra (Fig. 5(d)) in the mild region will be discussed later. With a fixed doping ratio, the device performance was enhanced from cold to mild, while decayed from mild to hot. Apparently, the J_{sc} was always improving as the temperature was increasing, which can be expected from the expanded crystalline grains. Larger grains with lower bulk defects can best boost the photogenerated carriers through the heterojunction. However, the preferable FF greater than 0.65 was obtained only in the mild region. Meanwhile, the dependence of V_{oc} on the temperature showed a similar variation with FF. For the mild region, the improved value of FF and V_{oc} than the cold region should be attributed to the ameliorative interface of perovskite/PCBM. Actually, this interfacial process is coupled with slow homogenization of a majority of loosely packed grains in the previously cold region. For the hot region, although the degree of crystalline was further extended, the infrequent areas of micro cracks and voids led to more internal shunting. Inevitably, the probability of charge trapping would be amplified. From all the

Table 1

The corresponding device parameters of the flexible solar cells in the ITO/PEDOT:PSS/modified α -FAPbI₃/PCBM/BCP/Ag configuration. (total 20 cells for each group).

Thermal region	Doping ratio	J_{sc} (mA/cm ²)	V_{oc} (V)	FF (%)	PCE (%)
Cold	1/5	18.11	0.95	64.4	11.08
	1/4	17.72	0.94	62.2	10.36
	1/3	13.44	0.94	64.9	8.19
	1/2	9.37	0.98	68.1	6.25
Mild	1/5	18.54	0.98	66.7	12.12
	1/4	18.26	0.99	68.6	12.41
	1/3	14.10	1.02	71.1	10.45
	1/2	10.28	1.09	70.7	7.92
Hot	1/5	18.76	0.96	62.9	11.33
	1/4	18.70	0.93	59.3	10.31
	1/3	15.09	0.94	55.5	7.88
	1/2	10.81	0.88	50.7	4.82

parameters discussed above, the size of crystalline grain is responsible for the PCE improvement (range: cold → mild) and the micro defect is in charge of the PCE degeneration (range: mild → hot). Consequently, the transforming mechanism of the perovskite films between the three thermal regions can be concluded in Fig. 5(e), which emphasizes the thermal energy on crystal growth kinetics. Considering the favorable crystalline grains and uniform morphology in the mild region, the optimal efficiency should be reached by virtue of the most beneficial exciton dissociation and diffusion.

Within the mild region, the flexible device performance generally declined as the doping ratio increased. The most distinguished PCE of 12.41% was yielded with a J_{sc} of 18.26 mA/cm², a V_{oc} of 0.99 V, a FF of 68.6% at the doping ratio of 1/4. Evidently, the solely reduction of J_{sc} was the main cause for the efficiency drop. Besides, the triumph values of the V_{oc} and the FF were attained at the highest doping ratio. The change of J_{sc} and V_{oc} along the doping ratio increased could be theoretically ascribed to the widened bandgap, which was also demonstrated by the prior absorption spectra of the perovskite films. Additionally, the chief reason for the elevated FF at the higher doping ratio was the

robust interface with enlarged crystal size. However, the flexible device based on the primitive α -FAPbI₃ exhibited a J_{sc} of 15.85 mA/cm², a V_{oc} of 0.96 V, a FF of 62.6% with a PCE of 9.53%. The result proves the agent MABr is indeed a pleasant assistant for α -FAPbI₃ and that the grain and lattice transformation can be hereby summarized as shown in Fig. 5(f). To get more insight of this mild agent, the external quantum efficiency (EQE) spectra (Fig. 5(d)) illuminated by monochromatic light were measured. Noticeably, the average EQE over a broad spectral range (330–780 nm) for the doping ratio of 1/5 and 1/4, reaching around 80%, overwhelmed the EQE for α -FAPbI₃. A positive EQE of about 75% was also observed for the doping ratio is 1/3 and an equivalent EQE was even obtained for the doping ratio is 1/2 until 600 nm. The improved photoresponse of the modified α -FAPbI₃ probably derives from the LUMO, which will prompt electron extraction to PCBM by lowering potential barrier. What's more, the wrought "pseudocubic" lattice by the MABr agent maybe also impacts the nature of the carriers transport. The integrated photocurrent densities from EQE are well matched with the J_{sc} .

Eventually, the supreme PCE of 13.03% (Fig. 6(a)) was realized at the 1/4 doping ratio in the mild region for the flexible solar cells, where the J_{sc} , V_{oc} and FF is 18.93 mA/cm², 0.994 V, 69.2%, respectively. The representative photograph of the bending flexible cell is presented in Fig. 6(a) inset. Meanwhile, the scan direction test was conducted for the hysteresis behavior (Fig. 6(a)). Negligible discrepancy was observed between FB-SC (from V_{oc} to J_{sc}) and SC-FB (from J_{sc} to V_{oc}) scans, which affirmed the modified lattice again. Moreover, the J-V characteristics in Fig. S7 demonstrated the PCE reduction of 0.18%, 0.61% and 0.81% at bending angles of 15°, 30° and 45° after 1000 times, respectively, which displayed admirable working ductility. Fig. 6(b) shows the favorable endurance by repeatedly bending of 45° for 1000 times.

For practical applications, the ultimate flexible devices should resist moisture well at room temperature in long term. Therefore, the stability of the optimal hybrid perovskite solar cells without encapsulation, which are exposed to 35% humidity in the dark, was estimated. As is shown in Fig. 7, the V_{oc} and FF almost remained except a little reduced J_{sc} . As a result, there was only a 1.03% drop of PCE in one month. For comparison, the device prepared by primitive α -FAPbI₃ exhibited striking decay of each parameter as time went by. After 30 days, a dreadful PCE of 0.68%

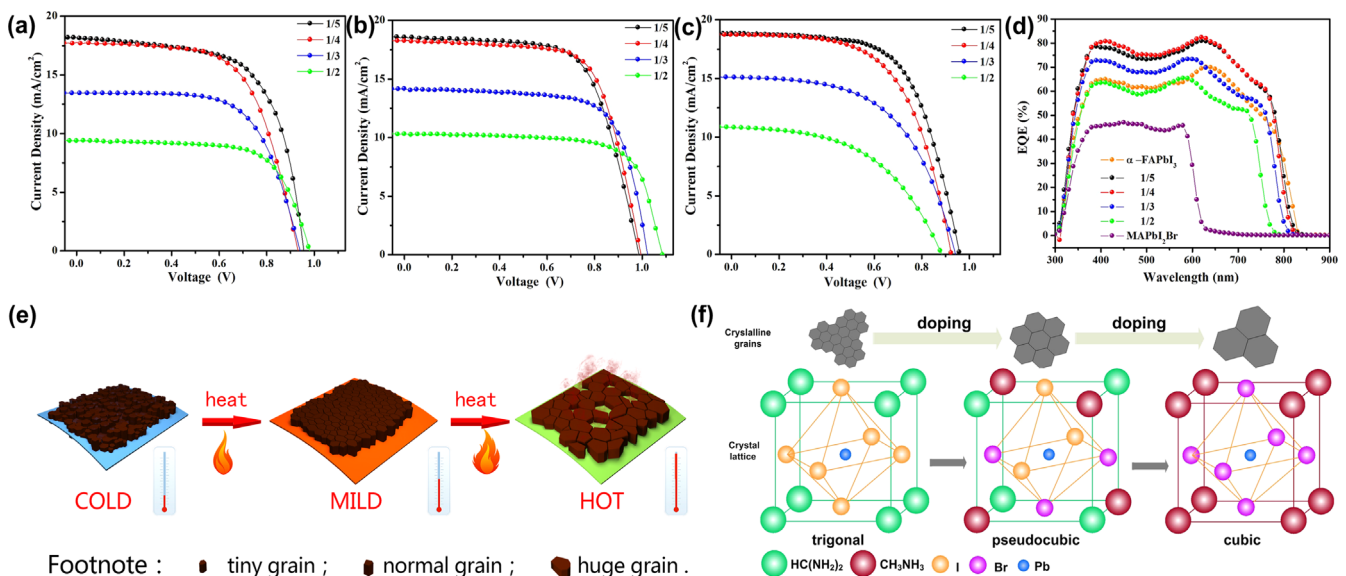


Fig. 5. Corresponding J-V characteristics of varied doping ratios in the three thermal regions: (a) the cold region, (b) the mild region and (c) the hot region. (d) The corresponding EQE spectra of the flexible devices in the mild region. (e) The transforming mechanism of the modified films by thermal energy. (f) The transforming mechanism of the modified films by doping ration.

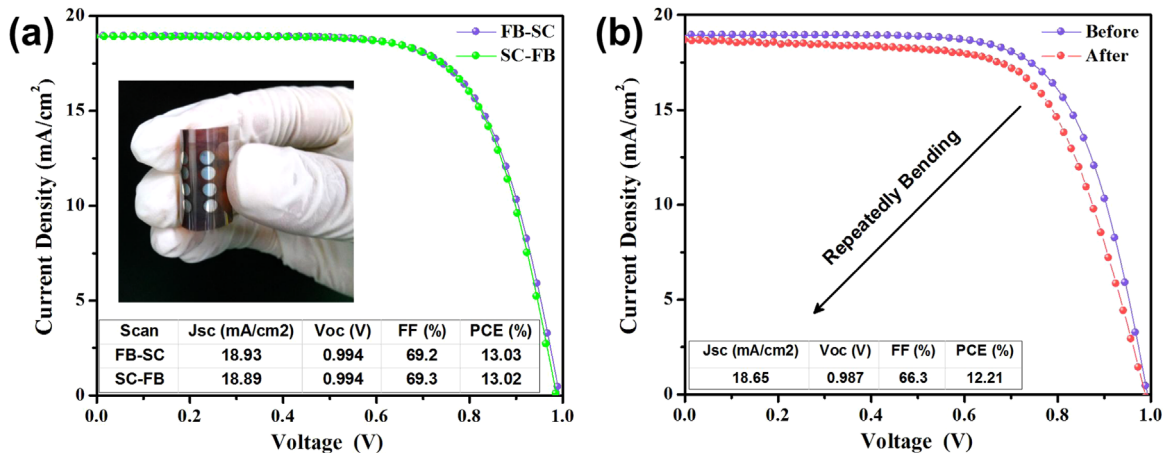


Fig. 6. (a) The *J-V* characteristics of the supreme flexible solar cells employing the suitable modified α -FAPbI₃. (b) The *J-V* characteristics after bending 45° for 1000 times.

was left with a faded perovskite film. Furthermore, the statistical analyses of the device parameters (including the PCE) for the improved devices before and after 1 month have been supplied in Fig. S8, according to our original experiment record of total 20 samples. The average primitive PCE of $12.41 \pm 0.52\%$ slightly reduced to $10.98 \pm 1.00\%$, proving the high-stability and reproducibility again. All the phenomena suggest that stable “pseudocubic” lattice assisted by the mild agent is in favor of the long term stability of flexible devices.

4. Conclusion

The thermal energy and the doping condition were thoroughly researched for the crystal growth kinetics of α -FAPbI₃. Lower temperature would retard the crystal growth and higher temperature would lead to over more micro voids. With EDX and TGA analysis, the thermal instability of the modified material should account for the poor morphology in the hot region. Furthermore, higher doping ratio of MABr benefited the crystalline grain due to

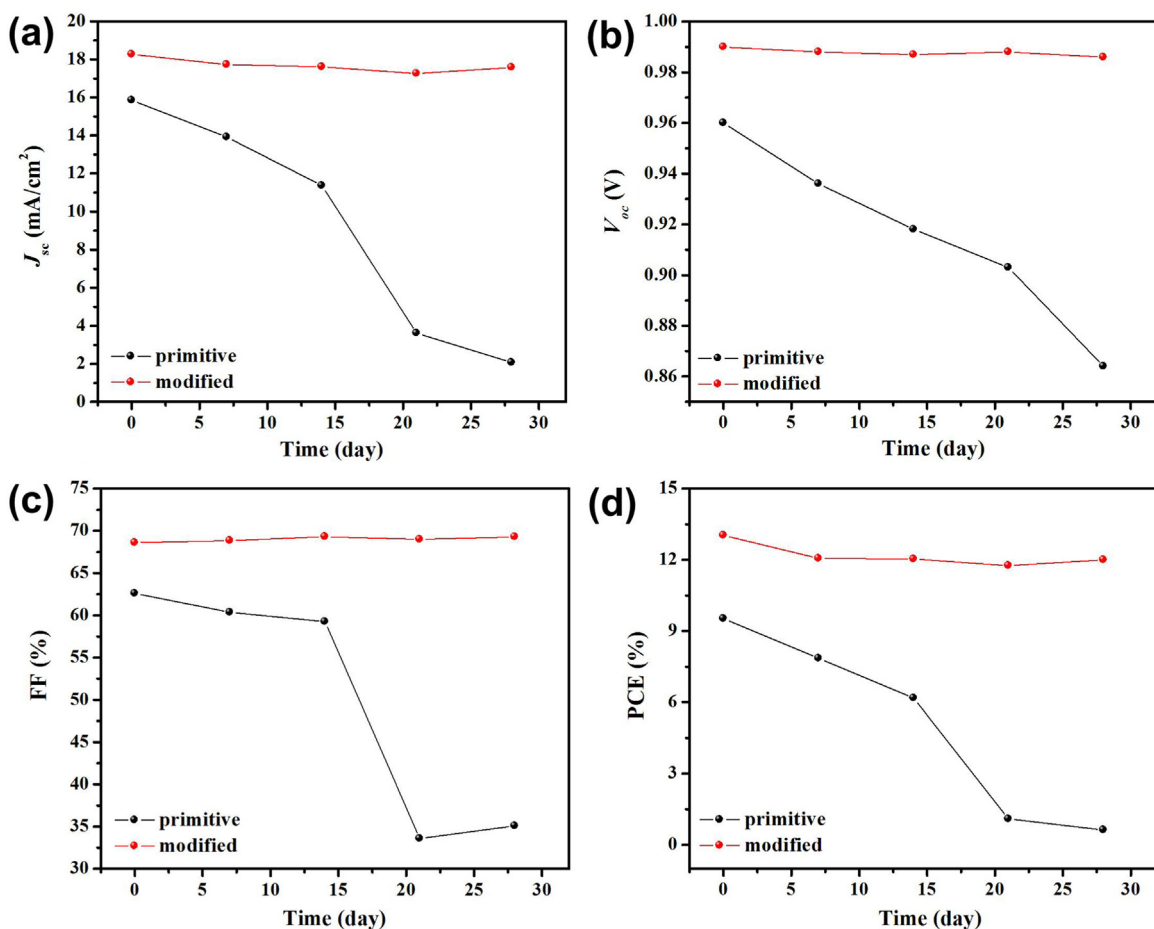


Fig. 7. The stability test at 35% humidity using the primitive α -FAPbI₃ and modified α -FAPbI₃ for the flexible devices. (a) J_{sc} , (b) V_{oc} , (c) FF and (d) PCE.

the preference of “pseudocubic” lattice. Ultimately, high efficiency and environmentally stable flexible solar cells based on the modified α -FAPbI₃ were successfully realized for the first time. The maximum PCE of 13.03% was obtained with the moderate doping ratio in the mild region. Meanwhile, the rosy flexible solar cell assisted by the mild agent showed super stable performance, suppressing the one with primitive α -FAPbI₃. It is hence believed that the stable flexible devices with large area will be expedited by this facile regulation of crystal growth.

Acknowledgment

This work was financially supported by Basic Research Program of China (2013CB328705), National Natural Science Foundation of China (Grant no. 11574248 and 61275034), Ph.D. Programs Foundation of Ministry of Education of China (Grant no. 20130201110065), International Cooperation by Shaanxi (Grant no. 2015KW-008). The SEM work was implemented at International Center by Dielectric Research (ICDR), Xi'an Jiaotong University, Xi'an, China. The authors also thank Ms. Dai for her help in using SEM.

Appendix A. Supplementary material

Supplementary data associated with this article can be found in the online version at <http://dx.doi.org/10.1016/j.nanoen.2016.06.007>.

References

- [1] A. Kojima, K. Teshima, Y. Shirai, T. Miyasaka, *J. Am. Chem. Soc.* 131 (2009) 6050–6051.
- [2] T. Leijtens, J. Lim, J. Teuscher, T. Park, H.J. Snaith, *Adv. Mater.* 25 (2013) 3227–3233.
- [3] S.D. Stranks, G.E. Eperon, G. Grancini, C. Menelaou, M.J.P. Alcocer, T. Leijtens, L.M. Herz, A. Petrozza, H.J. Snaith, *Science* 342 (2013) 341–343.
- [4] C. Wehrenfennig, G.E. Eperon, M.B. Johnston, H.J. Snaith, L.M. Herz, *Adv. Mater.* 26 (2014) 1584.
- [5] G. Xing, N. Mathews, S. Sun, S.S. Lim, Y.M. Lam, M. Grätzel, S. Mhaisalkar, T.C. Sum, *Science* 342 (2013) 344–347.
- [6] W.S. Yang, J.H. Noh, N.J. Jeon, Y.C. Kim, S. Ryu, J. Seo, S.I. Seok, *Science* 348 (2015) 1234–1237.
- [7] V.M. Goldschmidt, *Ber. Dtsch. Chem. Ges.* 60 (1927) 1263.
- [8] F. Hao, C.C. Stoumpos, R.P.H. Chang, M.G. Kanatzidis, *J. Am. Chem. Soc.* 136 (2014) 8094–8099.
- [9] Y. Ogomi, A. Morita, S. Tsukamoto, T. Saitho, N. Fujikawa, Q. Shen, T. Toyoda, K. Yoshino, S.S. Pandey, T. Ma, S. Hayase, *J. Phys. Chem. Lett.* 5 (2014) 1004–1011.
- [10] N.K. Noel, S.D. Stranks, A. Abate, C. Wehrenfennig, S. Guarnera, A.-A. Haghaghirad, A. Sadhanala, G.E. Eperon, S.K. Pathak, M.B. Johnston, A. Petrozza, L.M. Herz, H.J. Snaith, *Energy Environ. Sci.* 7 (2014) 3061–3068.
- [11] J.H. Noh, S.H. Im, J.H. Heo, T.N. Mandal, S.I. Seok, *Nano Lett.* 13 (2013) 1764–1769.
- [12] P.-W. Liang, C.-C. Cheuh, X.-K. Xin, F. Zuo, S.T. Williams, C.-Y. Liao, A.K.-J. Jen, *Adv. Energy Mater.* 5 (2015) 1400960.
- [13] Y. Zhao, K. Zhu, *J. Am. Chem. Soc.* 136 (2014) 12241–12244.
- [14] J. Qiu, Y. Qiu, K. Yan, M. Zhong, C. Mu, H. Yan, S. Yang, *Nanoscale* 5 (2013) 3245–3248.
- [15] R.W. Miles, *Vacuum* 80 (2006) 1090–1097.
- [16] C.C. Stoumpos, C.D. Malliakas, M.G. Kanatzidis, *Inorg. Chem.* 52 (2013) 9019–9038.
- [17] I. Borriello, G. Cantele, D. Ninno, *Phys. Rev. B* 77 (2008) 235214.
- [18] H. Zhou, Q. Chen, G. Li, S. Luo, T.-B. Song, H.-S. Duan, Z. Hong, J. You, Y. Liu, Y. Yang, *Science* 345 (2014) 542–546.
- [19] J.-H. Im, I.-H. Jang, N. Pellet, M. Grätzel, N.-G. Park, *Nat. Nanotechnol.* 9 (2014) 927–932.
- [20] N.G. Jeon, J.H. Noh, Y.C. Kim, W.S. Yang, S. Ryu, S.I. Seok, *Nat. Mater.* 13 (2014) 897–903.
- [21] J.-H. Im, J. Chuang, S.-J. Kim, N.-G. Park, *Nanoscale Res. Lett.* 7 (2012) 353.
- [22] D.B. Mitzi, K. Liang, *J. Solid State Chem.* 134 (1997) 376–381.
- [23] J.L. Knutson, J.D. Martin, D.B. Mitzi, *Inorg. Chem.* 44 (2005) 4699–4705.
- [24] T.M. Koh, K. Fu, Y. Fang, S. Chen, T.C. Sum, N. Mathews, S.G. Mhaisalkar, P. P. Boix, T. Baikie, *J. Phys. Chem. C* 118 (2014) 16458–16462.
- [25] G.E. Eperon, S.D. Stranks, C. Menelaou, M.B. Johnston, L.M. Herz, H.J. Snaith, *Energy Environ. Sci.* 7 (2014) 982–988.
- [26] F. Wang, H. Yu, H. Xu, N. Zhao, *Adv. Funct. Mater.* 25 (2015) 1120–1126.
- [27] J.-W. Lee, D.-J. Seol, A.-N. Cho, N.-G. Park, *Adv. Mater.* 26 (2014) 4991–4998.
- [28] N. Pellet, P. Gao, G. Gregori, T.-Y. Yang, M.K. Nazeeruddin, J. Maier, M. Grätzel, *Angew. Chem. Int. Ed.* 53 (2014) 3151–3157.
- [29] M. Hu, L. Liu, A. Mei, Y. Yang, T. Liu, H. Han, *J. Mater. Chem. A* 2 (2014) 17115–17121.
- [30] P. Docampo, J.M. Ball, M. Darwich, G.E. Eperon, H.J. Snaith, *Nat. Commun.* 4 (2013) 2761.
- [31] D. Liu, T.L. Kelly, *Nat. Photonics* 8 (2013) 133–138.
- [32] J. You, Z. Hong, Y. Yang, Q. Chen, M. Cai, T.-B. Song, C.-C. Chen, S. Lu, H. Zhou, Y. Yang, *ACS Nano* 8 (2014) 1674–1680.
- [33] B.J. Kim, D.H. Kim, Y.-Y. Lee, H.-W. Shin, G.S. Han, J.S. Hong, K. Mhmoed, T. K. Ahn, Y.-C. Joo, K.S. Hong, N.-G. Park, S. Lee, H.S. Jung, *Energy Environ. Sci.* 8 (2015) 916–921.
- [34] S.S. Shin, W.S. Yang, J.H. Noh, N.J. Jeon, J.H. Park, J.S. Kim, W.M. Seong, S.I. Seok, *Nat. Commun.* 6 (2015) 7410.
- [35] Y. Shao, Z. Xiao, C. Bi, Y. Yuan, J. Huang, *Nat. Commun.* 5 (2014) 5784.
- [36] Z. Xiao, Q. Dong, C. Bi, Y. Shao, Y. Yuan, J. Huang, *Adv. Mater.* 26 (2014) 6503–6509.
- [37] W. Zhang, M. Saliba, D.T. Moore, S.K. Pathak, M.T. Horantner, T. Stergiopoulos, S.D. Stranks, G.E. Eperon, J.A. Alexander-Webber, A. Abate, A. Sadhalana, S. Yao, Y. Chen, R.H. Friend, L.A. Estroff, U. Wiesner, H.J. Snaith, *Nat. Commun.* 6 (2015) 6142.
- [38] N.J. Jeon, J.H. Noh, W.S. Yang, Y.C. Kim, S. Ryu, S.I. Seok, *Nature* 517 (2015) 476–480.
- [39] S. Pang, H. Hu, J. Zhang, S. Lv, Y. Yu, F. Wei, T. Qin, H. Xu, Z. Liu, G. Cui, *Chem. Mater.* 26 (2014) 1458–1491.
- [40] H.-S. Kim, S.H. Im, N.-G. Park, *J. Phys. Chem. C* 118 (2014) 5615–5625.